energy&fuels

pubs.acs.org/EF

Article

Influence of Pore Morphology on Permeability through Digital Rock Modeling: New Insights from the Euler Number and Shape Factor

Xiangjie Qin, Yuxuan Xia, Jinsui Wu, Chenhao Sun, Jianhui Zeng, Kai Xu, and Jianchao Cai*

Cite This: *Energy Fuels* 2022, 36, 7519−7530

Read Online

ACCESS | Metrics & More | Article Recommendations

ABSTRACT: The microscopic pore shape and topology significantly affect fluid transport and occurrence in porous permeable rock. A quantitive characterization of the impact of pore morphology on permeability is currently lacking, which limits the efficient development of underground hydrocarbon resources. This work introduces the Euler number and shape factor to characterize the pore topology and shape of heterogeneous sandstone based on CT imaging. The pore morphology under different pore sizes and the correlation of the Euler number, shape factor, fractal dimension, and surface area are analyzed. Furthermore, a modified Kozeny−Carman equation is established to explain the influence of the Euler number and shape factor on permeability. The results show that with the increase of pore diameter, the Euler number decreases while the shape factor increases. In a connected pore system, the smaller Euler number corresponds to the complex pore network, which leads to the increase in the surface area, shape factor, and fractal dimension. At constant porosity, the shape factor is negatively correlated with permeability, and with increasing Euler number, the heterogeneity of the pore structure increases, resulting in an increase of flow resistance and a decrease of permeability. The results provide a new pore morphology characterization method for digital rock and help to understand the flow mechanism of hydrocarbons in complex pore networks.

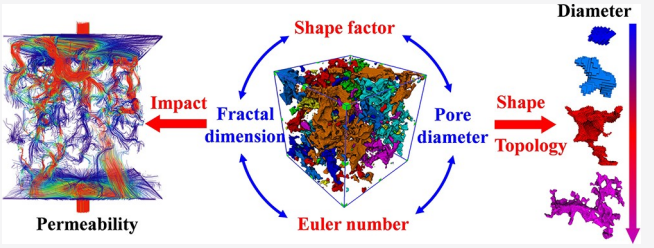

INTRODUCTION

The pore structure inside underground reservoir rock is the main space for hydrocarbon storage and migration.[1,2] In addition, microscopic petrophysical properties such as the pore morphology, pore size distribution (PSD), and permeability can provide an important basis for reservoir evaluation, development, and enhanced hydrocarbon recovery.[3,4] However, the microscopic pore structure of underground rock is complex, and the pore shapes and types are diverse, leading to an unclear fluid flow mechanism.[5−7] This limits the exploration and development of underground energy resources. Therefore, it is of great significance to characterize the pore shape and topology and in turn analyze their influence on permeability.

Numerical modeling is a common method to analyze the pore structure and predict the permeability of porous media, which is commonly divided into continuous scale and pore scale. The continuous-scale model based on the representative element volume can reasonably predict the macroscopic physical properties of porous media; however, the model size is much larger than the typical pore size of porous media, and the microscopic heterogeneity is ignored.[8] Pore-scale modeling can fully consider the microscopic heterogeneity and reasonably explore the microscopic pore shape and topology.[9−11] Digital rock reconstruction and modeling based on micro-CT images have become an important means to obtain the pore-scale microscopic properties.[12−14] One can obtain the three-dimensional (3D) pore system nondestructively and directly under a certain observation scale[15,16] and highly restore the real pore morphology compared with other observation methods such as focused ion beam scanning electron microscopy,[17,18] nuclear magnetic resonance spectroscopy,[19,20] and mercury intrusion porosimetry.[21] Raw CT images have strong postprocessability, and the target structure can be accurately extracted through image processing techniques.[22−24] Busse et al.[25] used unique image processing technology to extract the cleat structure in CT images and comprehensively characterized the cleat properties through cleat length, spacing, aperture, and connectivity. The structure obtained through 3D reconstruction can preserve real morphological characteristics. Wang et al.[26] introduced the shape factor to quantitatively characterize pore shape in coal and divided them into five types. They demonstrated that CT has advantages in the characterization of the pore shape. The fractal dimension describes the geometric shape and complexity of porous media. Rahner et al.[27] obtained the pore volume fractal dimension using a box-counting algorithm and PSD curves, characterized the pore morphology of sandstone and shale, and

Received: April 28, 2022
Revised: June 7, 2022
Published: July 5, 2022

https://doi.org/10.1021/acs.energyfuels.2c01359
Energy Fuels 2022, 36, 7519−7530

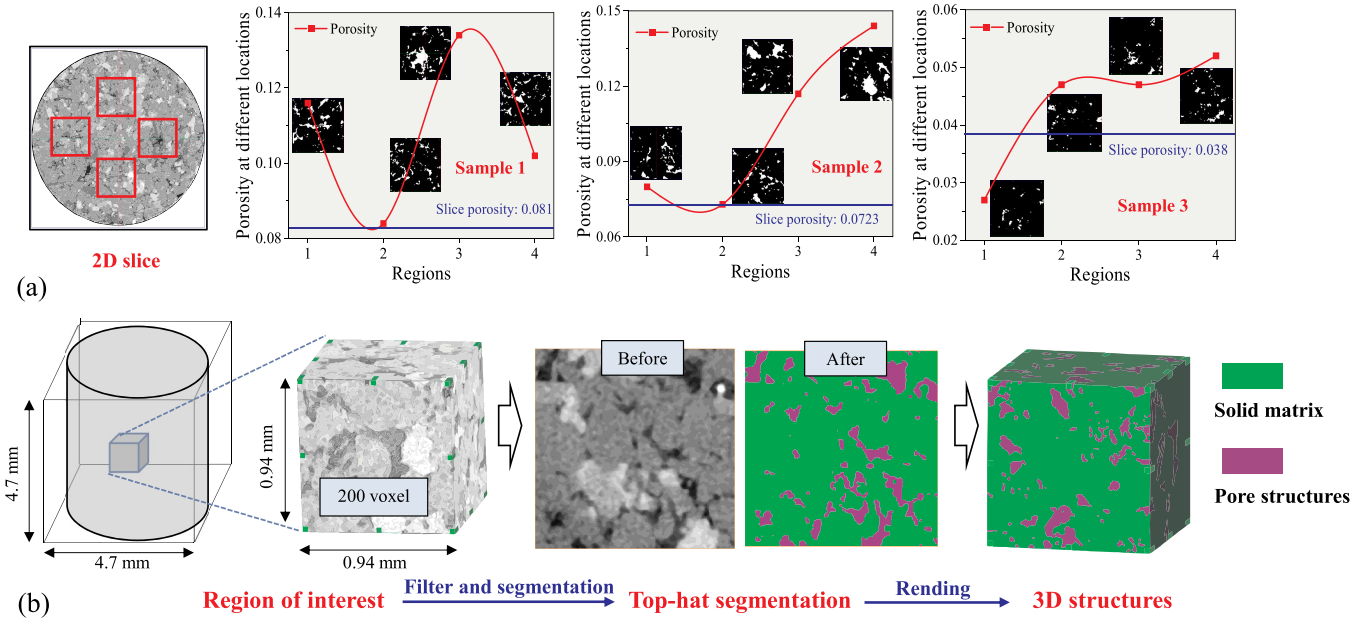

Figure 1. Model construction process: (a) heterogeneity of scanned samples and (b) reconstruction of CT images.

established the relationships between the fractal dimension, specific surface area, and porosity. Therefore, the pore structure properties, such as the surface area, porosity, pore size, and fractal dimension, can be obtained simply, nondestructively, and accurately based on CT imaging. However, the existing parameters cannot fully describe the complex pore topology due to pores that have different sizes and shapes being interconnected to form complex pore networks. The Euler number is commonly used to describe the object topology and has been gradually applied in digital rock analysis.[28] Li et al.,[29] Guo et al.,[30] and Yang et al.[31] used the Euler number to characterize the morphology of remaining oil in sandstone and combined the shape factor to divide the remaining oil into five types. Davudov et al.[32] illustrated that the Euler number can characterize the connectivity of the pore space and solid matrix; the smaller the Euler number, the better the connectivity. Guo and Cui[33] calculated the global Euler number of a rock matrix to reflect the pore connectivity; the smaller the Euler number, the better the connectivity. Besides, pores with complex networks may not provide sufficient flow channels. Most of these studies have used the Euler number as a global parameter to describe the connectivity of the pore space, but less attention has been paid to analyzing the pore topology quantitively, such as the corresponding PSD and the relationship between the Euler number and pore structure properties.

For the permeability characterization of CT-based digital rock, the connected pore system can be directly used as a geometric model to perform permeability simulation. Mostaghimi et al.[34] conducted a Stokes flow simulation on the binarized 3D image to obtain the permeability. They proved that the permeability difference of carbonate rock in different flow directions can be as high as 50%. In addition, Alhammadi et al.[35] improved the CT equipment and carried out the CT scanning experiment of water displacement under the steady state to obtain the relative permeability of carbonate rock and clarify the oil displacement mechanism in microscopic pores. As for the relationships between the permeability and pore structure properties, Wang et al.[36] analyzed coal heterogeneity based on PSD, investigated the influencing factors of permeability, and concluded that the fractal dimension is negatively correlated with the permeability. The simplified pore network model (PNM) can also be used to obtain the permeability. Yang et al.[37] established a PNM considering organic pores, obtained the permeability based on the modified single tube flow equation, and analyzed the influence of the slip length, viscosity ratio, and organic carbon content on permeability. In the above studies, the CT-based permeability was obtained through numerical and experimental methods, and the influencing factors of permeability were analyzed in detail. Nevertheless, the effect of pore morphology on permeability, such as the Euler number and shape factor of pore space, is ignored. In addition, a variety of factors affect the permeability of digital rock, and fewer studies have analyzed the relationship between the pore structure and permeability by controlling the variables. The Kozeny−Carman (KC) equation is widely applied in the prediction of permeability because it defines the quantitative relationship between the porosity and permeability, and the calculation is relatively simple.[38,39] Liu et al.[40] modified the KC equation by establishing a fractal model of the shape factor. Safari et al.[41] introduced eccentricity into the KC equation to correct the shape factor and combined discrete element analysis and LBM to simulate the permeability of different ellipsoid particles to verify the model. These studies have promoted the theoretical prediction of permeability, but the model parameters are mainly obtained through experiments or estimated using empirical equations. Micro-CT can directly obtain the 3D pore structure at a certain observation scale, and calculation of the parameters is accurate and straightforward. Therefore, the pore structure parameters obtained by the CT imaging technique can be combined with the theoretical model of permeability to analyze the influence of pore morphology on permeability under controlled variables.

In this work, the Euler number and shape factor are introduced to quantitatively characterize the pore shape and topology, and the corresponding PSD is analyzed, which expanded the application of CT imaging in pore morphology characterization. In addition, the relationships between the Euler number, shape factor, fractal dimension, and the surface

https://doi.org/10.1021/acs.energyfuels.2c01359
Energy Fuels 2022, 36, 7519−7530

area of connected pores are explored. By combing with digital rock reconstruction and simulation data, the KC equation is further modified to analyze the influence of the Euler number and shape factor on permeability under constant porosity. Thus, the fluid flow mechanism in pores with complex morphology is clarified.

2. MATERIALS AND METHODS

2.1. CT Scanning Experiments and Image Processing. Three sandstone samples from Dagang Oilfield were selected for this research, and the samples were polished into a cylinder with a diameter of 5 mm in the laboratory for the CT scanning experiment. A VerXRM-500 microscopic CT scanner manufactured by Zeiss with the scanning resolution of 4.7 μm was used, and the field of view is 4.7 mm in diameter and 4.7 mm in height.

One thousand one images were acquired from each sample after CT scanning. The large image size and wide range of gray value ($0-6.55 \times 10^4$) increase the amount of calculation during the analysis and simulation process. Thus, the original images were converted from 16 bits to 8 bits, and the corresponding gray value ranges from 0 to 255. Besides, it is found that the distribution of the microscopic pore structures in sandstone samples has strong heterogeneity as the pore structures from different regions (200 pixels × 200 pixels) at the same slice are significantly different (Figure 1a). Therefore, multiple pore-scale models with different pore structures can be constructed from the different regions of the CT images. The 3D reconstruction process of the target structure includes selection of the region of interest, image segmentation, and structure rendering (Figure 1b). First, four sets of CT images with different pore structures were cropped from the different regions of each sandstone sample, and 12 different models (S1−S12) were constructed with a model size of 200 × 200 × 200 voxels, corresponding to the actual size of 940 × 940 × 940 μm^3. The median filtering was then used to denoise the images, which can effectively remove a large number of randomly distributed noise.[42] Black Top-Hat segmentation can detect the dark area in grayscale images, corresponding to valleys, and a threshold can select the depth of valleys.[43] Therefore, it was used for image segmentation, and the microscopic pore properties were extracted. Finally, volume rendering was performed on segmented images to obtain the 3D target structure.

2.2. Permeability Simulation. Permeability simulation was performed using the connected pore system which was extracted through 26 neighborhoods method; elements connected to the points, lines, and faces of the cube voxel are considered to be interconnected. Figure 2a is the connected pore system after removing isolated pores.

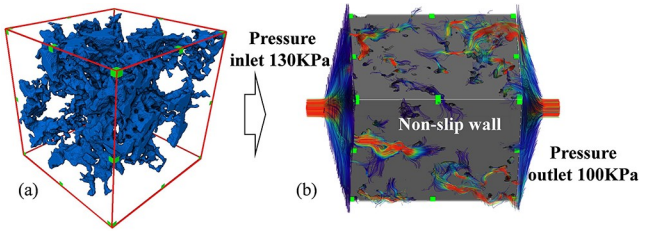

Figure 2. Schematic diagram of the permeability simulation: (a) connected pore system, (b) boundary conditions.

Each model was simulated in the *X*, *Y*, and *Z* directions based on the Navier−Stokes equation for the Newtonian incompressible fluids.[44,45] The fluid mode was laminar, and the fluid medium was defined as water with a dynamic viscosity of 0.001 Pa·s. The inlet and outlet pressures were 130 and 100 kPa, respectively. A voxel thickness wall defined as a nonslip wall (flow velocity at fluid boundary is 0) was set at the fluid boundary. In addition, solution iterations were set to 500−1 000 000 with the iteration error of 0.0001 to solve the Navier−Stokes equation and obtain the flow parameters. As a result, the permeability in three directions was calculated by Darcy's law, and the final value is the average. The reconstruction and simulation process was completed with AVIZO software. The permeability simulation method and boundary conditions are shown in Figure 2b.

2.3. Shape Factor. The pore surface area and diameter can be accurately obtained at a certain observation scale through the reconstructed 3D pore system. Under the specific pore volume, the larger the surface area, the more complex the shape is. With a certain surface area, the larger the volume, the simpler the shape is. Therefore, eq 1 can be used to characterize the pore shape.[46] When the shape factor is 1, the pore is spherical, and the larger the shape factor, the more complex the pore shape

$$S = \frac{A^3}{36\pi V_p^2} \tag{1}$$

where S is the shape factor, A is the pore surface area, and V_p is the pore volume.

2.4. Euler Number. Figure 3 displays the different pores in S1 under CT observation. It is found that a large number of holes exist in the pore structure, which damage the integrity of the pore space. With the variation of the pore volume, the number and size of holes are different, forming a complex pore network, resulting in a complicated mechanism of fluid occurrence and migration.

The Euler number is an important parameter to measure the topological structure.[25,32,47,48] Equation 2 shows how to calculate the Euler number

$$\chi(x) = \sum (-1)^r p(x) \tag{2}$$

where r is the spatial dimension, $\chi(x)$ is the Euler number of spatial target x, and $p(x)$ is the maximum number of r dimensional closed chains, also called the r-dimensional Betty number.

For 3D space, when $r > 2$, the value of the Betty number is 0, which has no practical significance. Therefore, one only needs to calculate the Betty number when $r \leq 2$. Equation 3 shows how to calculate the 3D Euler number[32]

$$E = \beta_0 - \beta_1 + \beta_2 \tag{3}$$

where E is the 3D Euler number, β_0 is the number of isolated components, β_1 is the number of channels, and β_2 is the number of closed cavities.

Digital rock contains a pore phase and a solid phase. Figure 4 is the schematic illustration of the calculation method of the Euler number for solid phase. It uses the number of isolated components (1 for a single target) minus the number of channels plus the number of enclosed cavities (i.e., isolated pores). Therefore, the smaller the Euler number, the greater the number of fluid channels, the lower the number of isolated pores are, and the better the connectivity is. In addition, the pore connectivity can also be characterized by calculating the global Euler number of the total pore system. A smaller Euler number value corresponds to a smaller number of isolated pores and stronger connectivity.

The Euler number was introduced to describe the 3D pore topology. In this situation, the number of isolated components is 1, the channels are the holes in the pore structure (Figure 3), and the number of closed cavities is 0. Therefore, the smaller the Euler number, the more holes there are in pore structure, and the more complex the topology. The maximum Euler number is 1, which means there is no hole in the pore structure.

2.5. Fractal Dimension. The fractal dimension characterizes the complexity of the pore structure quantitively, and it is generally distributed around 2−3 for the 3D pore system.[49] The larger the value, the more complex the structure is.[50,51] The fractal dimension was obtained through the box-counting algorithm

$$D = \lim_{\varepsilon \to 0} \frac{\ln N(\varepsilon)}{\ln \frac{1}{\varepsilon}} \tag{4}$$

where D is the pore volume fractal dimension, ε is the side length of the cube box, and $N(\varepsilon)$ is the number of boxes with side length ε.

2.6. Characterization of the Permeability. The permeability of digital rock is generally obtained by numerical simulation, where it is

https://doi.org/10.1021/acs.energyfuels.2c01359
Energy Fuels 2022, 36, 7519−7530

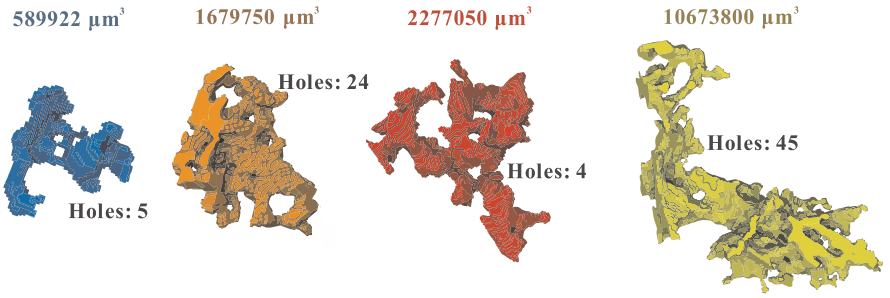

Figure 3. Holes in pore structures with different volumes.

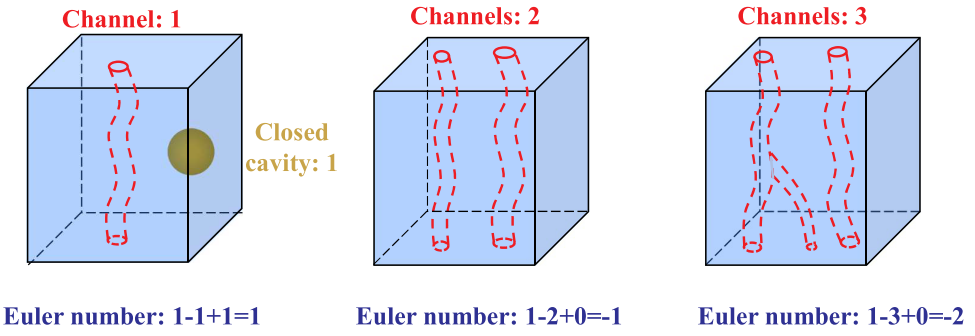

Figure 4. Calculation principle of the Euler number.

difficult to control the variables when analyzing the relationship between the pore structure properties and permeability, and there is a lack of theoretical prediction of the permeability. The KC equation is widely used in permeability prediction; it describes the quantitative relationship between the permeability, porosity, and specific surface area (eq 5).[52] However, the KC constant is related to the pore structure properties,[53,54] and it is not a definite value

$$K = \frac{K_c \varphi^3}{M^2} \tag{5}$$

where K_c is the KC constant, φ is the porosity, and M is the specific surface area, which is the ratio of the pore surface area to the model volume.

The KC equation was introduced to estimate the permeability of CT-based digital rock. First, the simulated permeability was combined with eq 5 to obtain the KC constant (the porosity and specific surface area can be accurately obtained through 3D pore structure analysis). Then, the quantitative relationship between the KC constant and pore structure parameters was established through multiple regression to modify the KC equation. Finally, the influence of the pore morphology on permeability was analyzed.

3. RESULTS AND DISCUSSION

3.1. Measurement of the Euler Number and Shape Factor. The shape factor is generally calculated from the ratio of the pore surface area to volume (eq 1). Euler number can be obtained by counting the number of isolated components, holes, and closed cavities in combination with eq 3. Their calculations were all completed using AVIZO software. Moreover, the shape factor can be accurately calculated due to the advantages of CT imaging in pore volume and surface area measurements. In addition to the Euler number calculation method in eq 3, another interesting method is mentioned in Davudov's work.[32] It uses the number of isolated components minus the number of redundant pore system connections plus the number of enclosed cavities. The PNM constructed by the connected pore system based on the watershed algorithm was used to develop this method and calculate the corresponding Euler number. Pore throats in the PNM are interconnected; thus, the number of isolated components is 1, and the number of closed cavities is 0. The number of redundant pore system connections can be obtained by subtracting the throat number minus the pore number plus 1. Therefore, the smaller the Euler number, the greater the number of redundant throats and the stronger the pore connectivity. It is found that the Euler number calculated by the connected pore system is consistent with the Euler number calculated by the PNM (Figure 5), which verifies the accuracy of the calculation. Besides, the Euler number calculated by the PNM is about 0.6 times that of the connected pore structure. This is because the pore-throat number in the PNM depends on the model construction method. It is worth noting that calculation of the shape factor and Euler number is

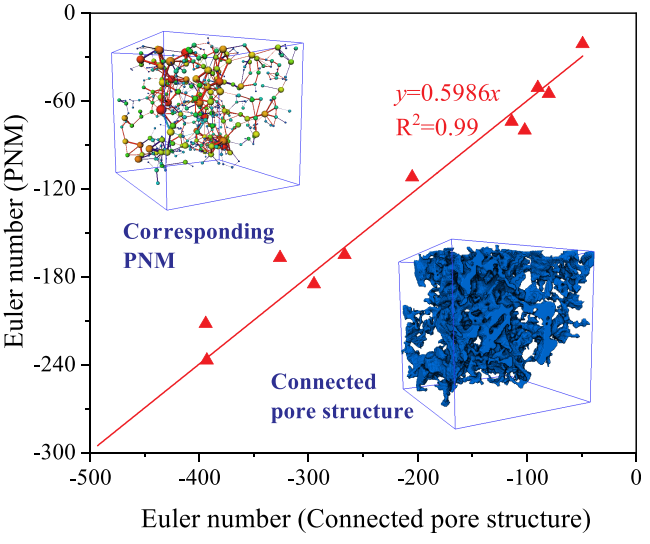

Figure 5. Comparison of the Euler number obtained through the two methods.

https://doi.org/10.1021/acs.energyfuels.2c01359
Energy Fuels 2022, 36, 7519−7530

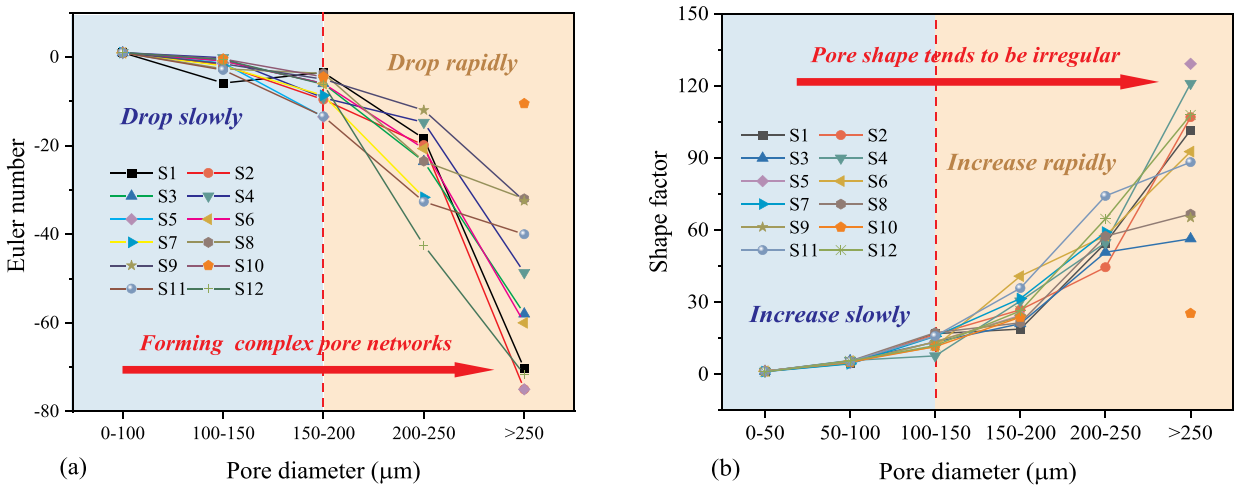

Figure 6. Euler number and shape factor distribution in different pore diameters of 12 models: (a) Euler number, (b) shape factor.

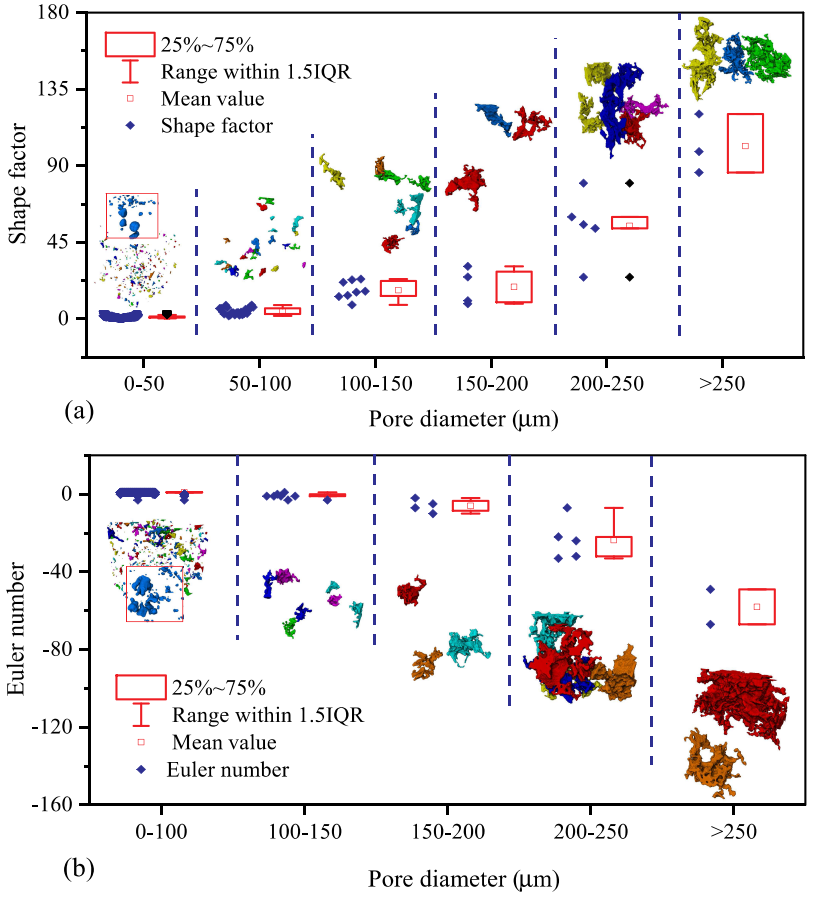

Figure 7. Pore morphology distribution characteristics: (a) shape factor distribution in S1 and (b) Euler number distribution in S3.

performed on digital cores, which is also applicable to conventional and unconventional digital rocks such as carbonate, shale, and coal.

3.2. Pore Shape and Topology with Different Pore Sizes. The Euler number and shape factor calculated in different pore sizes of the 12 models were used to explore the pore morphology distribution (Figure 6). The pore diameter was calculated based on a spherical shape due to the large difference in pore shape. In addition, the Separate Objects module was used to calculate the watershed line in binary images to separate the pore space and obtain more pores. Figure 6a shows the changing characteristics of the Euler number, which gradually decreases with increasing pore diameter. The larger the pore diameter, the faster the Euler number decreases and the greater the difference in Euler number. This means that with increasing pore volume, there are more holes in pore structure, forming a complex pore network. The larger the pore volume is, the more significant the difference in topology among the different pores. As displayed in Figure 6b, the shape factor increases as the pore diameter increases, and in most models, the larger the pore diameter, the faster the shape factor increases. This demonstrates that the pore shape tends to be complex with increasing

https://doi.org/10.1021/acs.energyfuels.2c01359
Energy Fuels 2022, 36, 7519−7530

pore volume, and the larger the pore volume is, the more significant the difference in pore shape. In addition, the shape factor and Euler number show opposite trends with the variation of pore diameter, indicating that with increasing pore volume the number of holes in the pore structure increases, forming a complex pore shape and network.

Box plots were developed to analyze the distribution of the Euler number and shape factor and further explore the pore morphology characteristics; it can intuitively display the pore number, shape factor, and Euler number values in a specific pore diameter range. Besides, the top and bottom of the box represent the maximum and minimum values of the data (except outliers), respectively, and the mean value is also given inside the box. Figure 7a displays the distribution of the shape factor in S1. In the pore diameter range of 0−50 μm, the pore number is 346, the average shape factor is 1.14, most of pores are nearly spherical, and the maximum shape factor is 4.47. In the range of 50−100 μm, the pore number is 23, the average shape factor value is 4.46, and the maximum and minimum values are 8.12 and 1.78, respectively. In the range of 100−150 μm, the average shape factor is 16.85 and the maximum and minimum values are 8.2 and 23.3, respectively. When the pore diameter is greater than 250 μm, there are only 3 pores and the average shape factor is 101.6. Therefore, with increasing pore diameter, the pore number decreases and the pore shape becomes more irregular. The larger the pore diameter, the greater the difference in pore shape between different pores. Figure 7b shows the pore structures and the corresponding Euler number in S3. With a pore diameter of 0−100 μm, there are 465 pores, most of which have a Euler number of 1 and an average value of 0.96. This demonstrates that the pore structure is complete. Only one pore has a smaller Euler number, which is −3. With a pore diameter of 100−150 μm, the pore number is 7 and the Euler number of most pores is less than 0 with an average Euler number of −0.86. With pore diameters of 150−200 μm, the pore number is 4 with an average Euler number of −6 and the maximum and minimum Euler number are −2 and −10, respectively. When the pore diameter is greater than 250 μm, there are only 2 pores, the pore diameters are 253.66 and 497.29 μm, and the corresponding Euler numbers are −49 and −67, respectively. Therefore, with increasing pore diameter, the number of holes in pore structure increases and the topology tends to be complex. The larger the pore diameter is, the greater the difference in Euler number. This demonstrates that the larger the pore diameter is, the more obvious the difference of morphology, which leads to a larger difference in Euler number and shape factor between different models (Figure 6). For example, S10 has no pore distribution in the range of 200−250 μm and strong heterogeneity, leading to the significant difference from other models.

3.3. Correlation of the Pore Structure Properties. There are many isolated pores in the total pore system, and the pore volume fraction that was extracted directly from the 3D image after image segmentation was used to analyze the connected and isolated pore distribution (Figure 8). The volume fraction of connected pore is the largest, and the volume fraction of isolated pores is smaller. As the pore diameter increases, the pore distribution becomes discrete. The volume fraction of the connected pore in S1 is 0.093 with a diameter of 530.78 μm. The diameters of isolated pores are all less than 150 μm, and the volume fraction is only 0.01. Therefore, the proportion of isolated pores is smaller, only the connected pore contributes to permeability, and the correlation analysis was carried out using the connected pore structures.

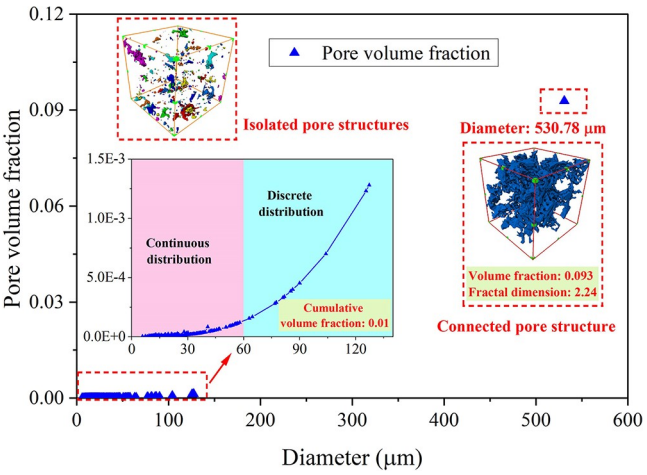

Figure 8. Distribution of connected and isolated pores in S1.

The connected pore system of 12 models was extracted (Figure 9a), and the Euler number, shape factor, surface area, fractal dimension, and pore diameter were calculated to describe pore morphology quantitatively. In order to intuitively display the porosity distribution of these models and preliminarily study the relationship between the porosity and pore morphology, Figure 9b displays the pore structure parameters with increasing porosity; the corresponding models are S11, S5, S10, S8, S6, S9, S7, S4, S1, S2, S12, and S3 in sequence. The porosity of sandstone is low, 7 models have a porosity of less than 6%, and 5 models have a porosity of greater than 6%. The porosity is positively correlated with the pore diameter, surface area, fractal dimension, and shape factor, and negatively correlated with the Euler number. The variation of the pore diameter has a certain difference with the surface area since the surface area is obtained based on the actual pore geometry. S3 has the largest pore diameter, and S12 has the largest surface area, indicating that the pore morphology of S12 is heterogeneous. The fractal dimension between these models is quite different; S11 has the lowest fractal dimension (2.04), and S12 has the highest fractal dimension (2.27). The variation of the Euler number and shape factor is opposite, indicating that a smaller Euler number corresponds to a complex pore network, which leads to an increase in shape factor. Among them, S12 has the largest shape factor (865.30) and the smallest Euler number (−493), and S10 has the smallest shape factor (137.08) and the largest Euler number (−49).

The Pearson matrix was established to quantitatively analyze the correlation as mentioned in Figure 9b, and all input parameters are significantly correlated (Figure 9c). The shape factor, surface area, pore diameter, porosity, and fractal dimension are positively correlated and negatively correlated with the Euler number. The positive correlation between the pore diameter and porosity is the strongest since the pore diameter is calculated based on pore volume. The Euler number has the strongest negative correlation with the shape factor and surface area followed by fractal dimension with correlation coefficients of 0.95, 0.95, and 0.91, respectively, meaning that a change of the Euler number has a significant influence on the shape and heterogeneity of pore space. The shape factor has a significant positive correlation with the surface area and fractal dimension, and the correlation coefficients are 0.89 and 0.83, respectively. Besides, the porosity is negatively correlated with the Euler number and positively correlated with shape factor.

https://doi.org/10.1021/acs.energyfuels.2c01359
Energy Fuels 2022, 36, 7519−7530

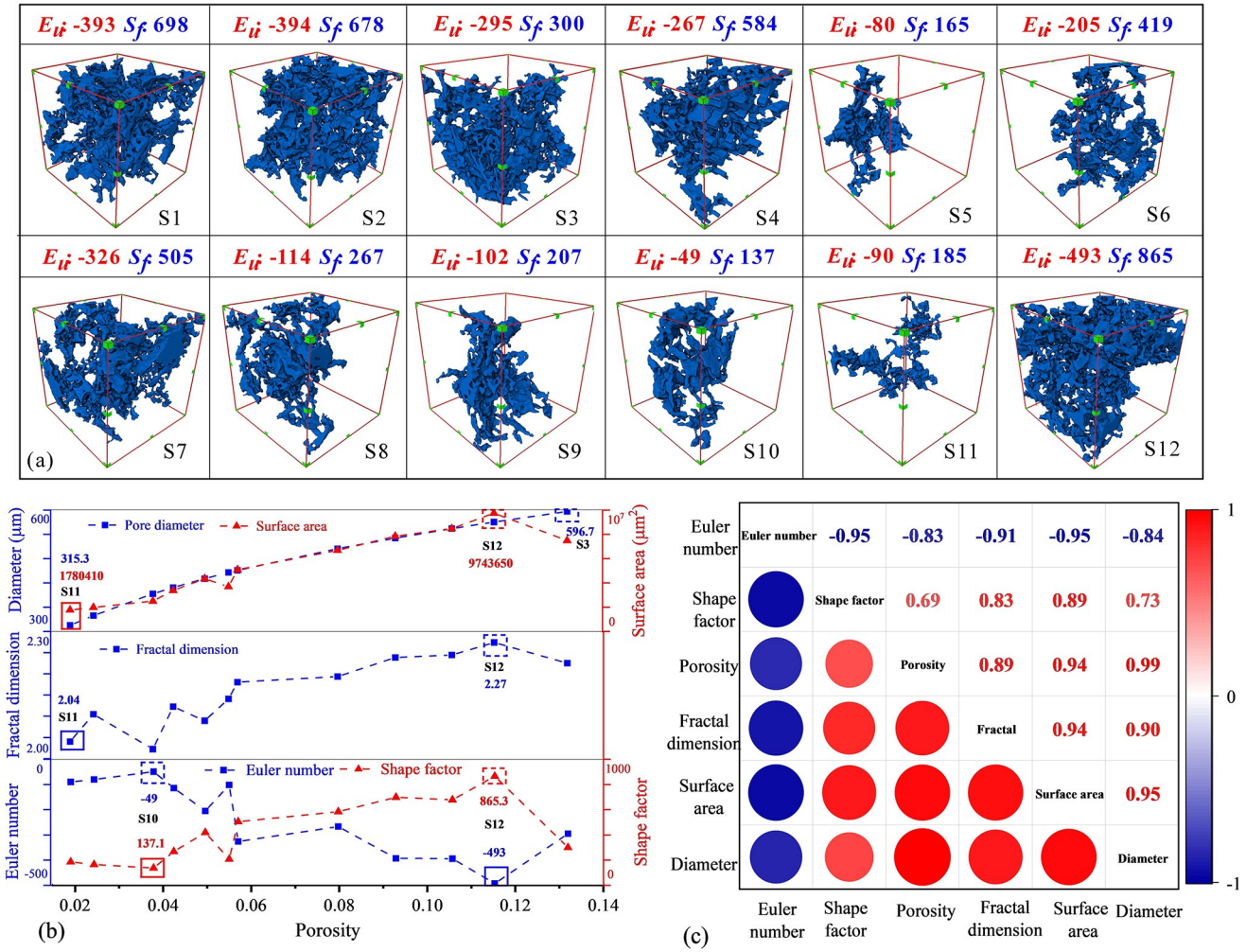

Figure 9. Correlation of the pore structure properties: (a) connected pore structures, (b) pore structure parameters, and (c) correlation matrix.

This indicates that with increasing pore volume, the number of holes in pore network increases (Euler number decreases), resulting in a complex pore shape and network (shape factor and fractal dimension increase) and increased pore surface area.

The porosity significantly affects the correlation between the pore morphological parameters since it is related to the Euler number, shape factor, fractal dimension, and surface area. In this context, partial correlation analysis (eq 6) was introduced to eliminate the influence of porosity, and Table 1 shows the corresponding analysis results. The correlation does not change greatly; the coefficients changed only after removing the influence of porosity. This is because the pore morphology has a strong correlation with porosity, and the coefficients will change significantly when the influence of porosity is excluded. The correlation coefficient between the shape factor and surface area is close to 1, which corresponds to the calculation of shape factor (eq 1), and the accuracy of partial correlation analysis is verified. The Euler number is still strongly negatively correlated with the shape factor and surface area with correlation coefficients of 0.925 and 0.900, respectively. However, their correlation with the fractal dimension is weakened significantly; coefficients are lower than 0.7. This explains why the decrease of Euler number increases the number of holes, forming a dense and complex pore network, resulting in the increase of the pore surface area, shape factor and fractal dimension

Table 1. Partial Correlation Analysis Results with Constant Porosity

parameter	coefficient	fractal dimension	Euler number	shape factor	surface area
fractal dimension	correlation	1.000	−0.670	0.649	0.653
	significance	0.000	0.024	0.031	0.029
Euler number	correlation	−0.670	1.000	−0.925	−0.900
	significance	0.024	0.000	0.000	0.000
shape factor	correlation	0.649	−0.925	1.000	0.996
	significance	0.031	0.000	0.000	0.000
surface area	correlation	0.653	−0.900	0.996	1.000
	significance	0.029	0.000	0.000	0.000

$$r_{12(3)} = \frac{r_{12} - r_{13}r_{23}}{\sqrt{1 - r_{13}^2}\sqrt{1 - r_{23}^2}} \quad (6)$$

where $r_{12(3)}$ is the correlation coefficient between x_1 and x_2 after removing the influence of x_3, r_{12} is the correlation coefficient between x_1 and x_2, r_{13} is the correlation coefficient between x_1 and x_3, and r_{23} is the correlation coefficient between x_2 and x_3.

3.4. Quantitative Characterization of the Permeability. Figure 10 displays the permeability results simulated using connected pore structures in the *X*, *Y*, and *Z* directions with the

https://doi.org/10.1021/acs.energyfuels.2c01359
Energy Fuels 2022, 36, 7519−7530

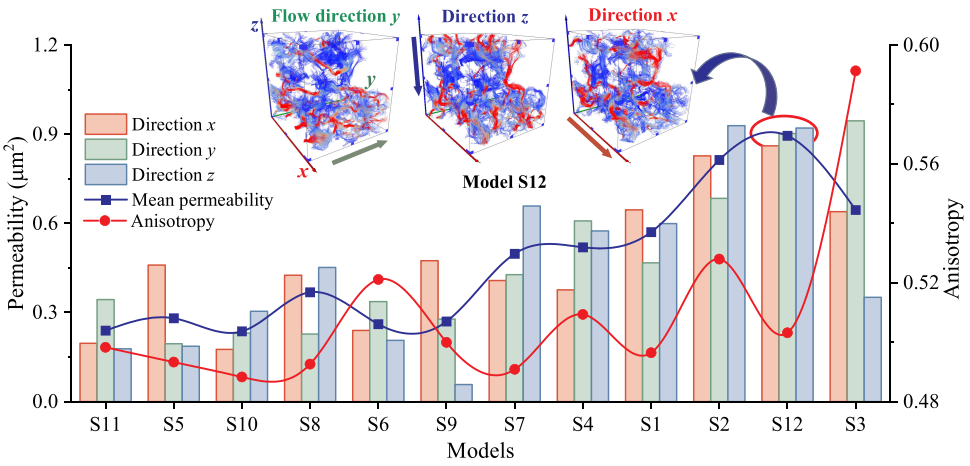

Figure 10. Permeability and anisotropy of the 12 models.

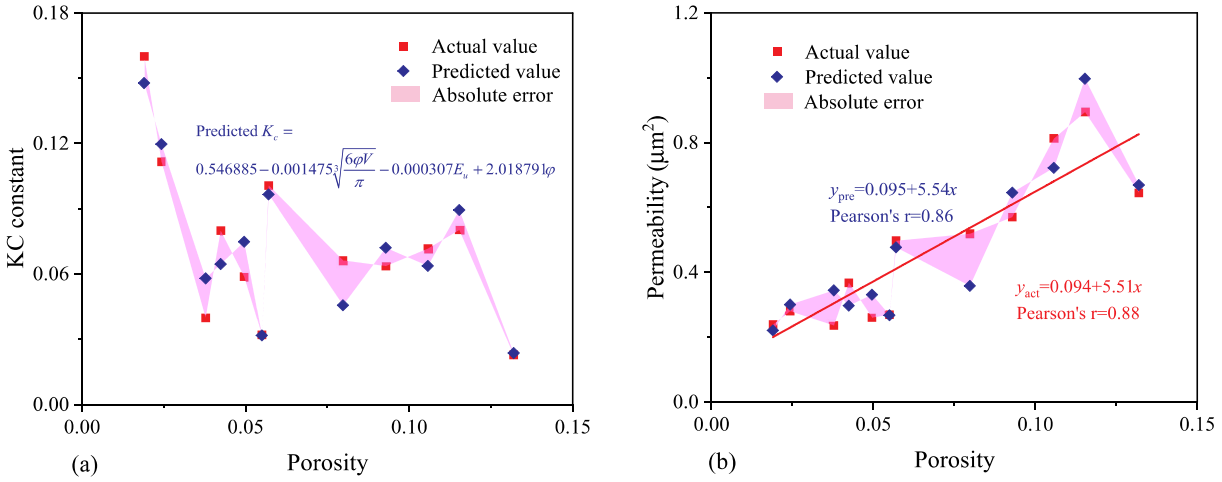

Figure 11. KC constant and permeability prediction results: (a) KC constant, (b) permeability.

corresponding mean permeability and anisotropy. Anisotropy (A_n) was obtained by emitting a set of rays at different angles to the corresponding binary image of the connected pore system. The length of the intersection of each ray with the object encountered was measured, and the distribution of the mean intercept length was analyzed via an eigenvalue decomposition. The ratio of the minimum and maximum eigenvalues (λ_{min}, λ_{max}) can be used to characterize the anisotropy (eq 7)

$$A_n = 1 - \frac{\lambda_{min}}{\lambda_{max}} \tag{7}$$

The connected porosity of these models is in the range of 1.9−13.2%, and the corresponding mean permeability is 0.237−0.895 μm^2 (Figure 10). Due to the limitations of image resolution and simulation scale, the tiny pores have not been effectively observed, resulting in the higher permeability obtained by simulations.[55] All of the connected pore structures are anisotropic, ranging from 0.488 to 0.591, with different permeability in three directions. The anisotropies of S2, S3, S4, and S6 are strong, and the corresponding values are higher than 0.5. The permeability increases with increasing porosity. S12 has the highest mean permeability with a higher porosity and fractal dimension of 11.5% and 2.274, respectively. In addition, the permeability of S12 in three directions is similar, and the anisotropy is relatively weak. S3 has the highest permeability in the Y direction but the strongest anisotropy, resulting in low permeability in the X and Z directions and low mean permeability. S10 has the lowest permeability with a lower porosity and the lowest fractal dimension of 3.8% and 2.022, respectively. Therefore, the porosity, fractal dimension, and anisotropy are closely related to permeability.

The simulated mean permeability, porosity, and specific surface area were combined with eq 5 to obtain the KC constant, which fluctuates widely and distributes from 0.023 to 0.160 (Figure 11a). Compared with the connected pore structures (Figure 9), the KC constant of S11 is the largest, followed by S5, and their corresponding porosity is smaller, being 1.9% and 2.4%, respectively. The KC constant of S3 is the smallest, and the corresponding porosity is the largest, which is 13.2%. The KC constants of S3 (0.023), S9 (0.032), and S10 (0.04) are close, but the porosities of S9 and S10 are lower, being 5.5% and 3.8%, respectively. Although the maximum and minimum values of the KC constant correspond to the minimum and maximum values of the porosity, respectively, they are generally weakly correlated. In order to further analyze the relationships between the KC constant and pore structure (porosity, fractal dimension, anisotropy, Euler number, shape factor, pore area, pore diameter), the corresponding Pearson correlation matrix is established. The results indicate that the KC constant is negatively correlated with the pore diameter, with a correlation coefficient of 0.58. In general, the bivariate correlation between

https://doi.org/10.1021/acs.energyfuels.2c01359
Energy Fuels 2022, 36, 7519−7530

the KC constant and the pore structure are poor, and the KC constant may be controlled by multiple parameters.

Multiple regression was introduced to establish the quantitative relationship between the pore structure and KC constant. The dependent variable was set as the KC constant, and the independent variables were determined to be the porosity, fractal dimension, anisotropy, Euler number, shape factor, surface area, and pore diameter. The regression method was set to step to automatically select the closely related variables, remove the remaining variables, and output the quantitative relationship (Table 2). Three models were output

Table 2. Multiple Regression Fitting Results

model	R^2	standard skewness error	parameter	coefficient	significance
1	0.338	0.0321	constant	0.185368	0.004
			pore diameter	−0.000241	0.047
2	0.781	0.0194	constant	0.310771	0.000
			pore diameter	−0.000671	0.000
			Euler number	−0.000312	0.002
3	0.891	0.0146	constant	0.546885	0.000
			pore diameter	−0.001475	0.000
			Euler number	−0.000307	0.001
			porosity	2.018791	0.022

after iteration with fitting degrees of 0.338, 0.781, and 0.891. The model with the highest fitting degree was selected to characterize the KC constant, which can be quantitatively described by the linear relationship of the pore diameter, Euler number, and porosity. The variance inflation factor values of all variables are less than 10, satisfying colinear diagnosis, and the significance of each coefficient is less than 0.05, so the output regression model is statistically significant. Since the pore diameter is calculated from the pore volume and can be obtained from the porosity, the KC constant can be described by the porosity and Euler number (eq 8)

$$K_c = 0.546885 - 0.001475\sqrt[3]{\frac{6\varphi V}{\pi}} - 0.000307E + 2.018791\varphi \quad (8)$$

where V is the model volume.

Combining the shape factor (eq 1) and KC constant (eq 8) with eq 5, a relationship between the porosity, Euler number, and shape factor and permeability can be obtained (eq 9)

$$K = \frac{\sqrt[3]{V^2}(l + m\sqrt[3]{\varphi V} + nE + h\varphi)\sqrt[3]{\varphi^5}}{\sqrt[3]{(36\pi \cdot S)^2}} \quad (9)$$

where l, m, n, and h are fitting parameters, which may relate to the image resolution since the permeability of digital rock with different resolutions is quite different.

The predicted (multiple regression fitting results) and actual values of the KC constant are compared in Figure 11a, indicating that the error is reasonable, with the mean absolute and relative errors being only 0.01 and 0.15, respectively, and the absolute error of most models is less than 0.01. The prediction is the worst when the porosity is 0.79 (model S4), with an absolute error of 0.02. In addition, the permeability calculation results based on eq 9 are compared in Figure 11b. S4 has the worst predicted permeability with an actual value of 0.52 μm^2 compared to the predicted value of 0.36 μm^2, but the overall prediction is reasonable with an average absolute error of 0.06 μm^2. The relationship between the porosity and permeability shows a positive correlation in both actual and predicted values with corresponding correlation coefficients of 0.88 and 0.86, respectively, and the linear relationships between the two basically coincide. Therefore, the modified KC equation can reasonably characterize permeability based on the obtained data and can be used to further analyze the effect of pore morphology on permeability.

3.5. Influence of Pore Morphology on Permeability.

The influence of the pore structure on permeability directly obtained without controlling variables is poor under micro-CT observation since many factors affect permeability. The modified KC equation can reasonably characterize the permeability of porous digital rock, which is obtained based on 12 heterogeneous sandstone models. Therefore, the influence of the pore morphology (shape factor and Euler number) on permeability can be obtained by controlling variables based on eq 7. Figure 12 displays the influence of the Euler number and shape factor on permeability when the porosity is 0.05 and the shape factor is in the range of 0−1000. With increasing shape factor, the shape of the connected pore is complicated and the permeability decreases. The larger the shape factor, the slower the rate of permeability decreases. The

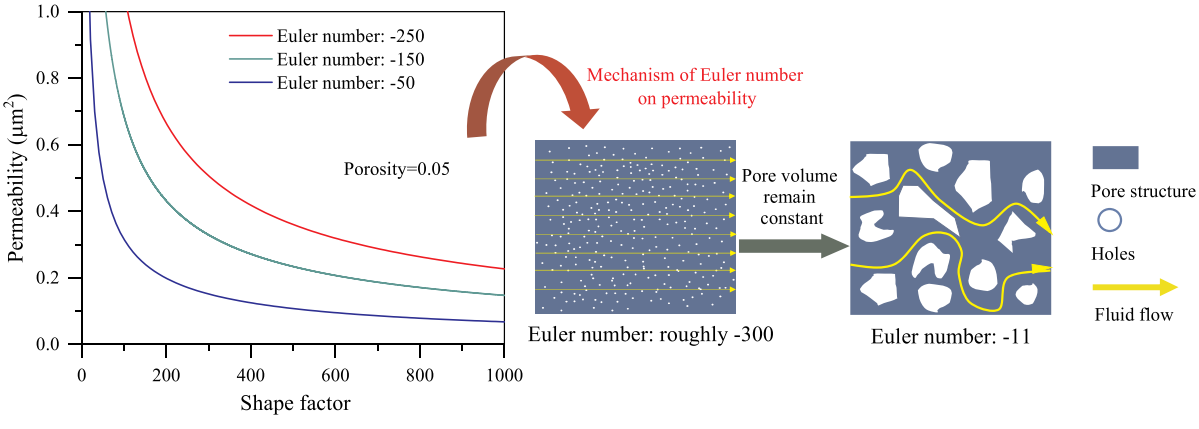

Figure 12. Influence of the pore morphology on permeability under constant porosity.

https://doi.org/10.1021/acs.energyfuels.2c01359
Energy Fuels 2022, 36, 7519−7530

influence of the shape factor on permeability is more obvious when the Euler number is larger. The Euler number has a negative correlation with permeability. The larger the shape factor, the smaller the influence of the Euler number on permeability. In addition, the effect of the Euler number on permeability was analyzed when the porosity and shape factor remain unchanged (Figure 12). There are a large number of holes in the connected pore structure when the Euler number is small. As the Euler number increases, the number of holes decreases, small holes merge into large holes, and the shape of the holes becomes complicated as the volume and surface area remain unchanged, resulting in increased heterogeneity of the pore structure, which in turn leads to the complicated fluid flow and reduced permeability.

The microscopic pore morphology has a significant impact on permeability, and the permeability can be preliminarily estimated by the Euler number and shape factor, which provides a new reference for accurate prediction of permeability. Although the applicability of this conclusion to ultralow permeability rocks is uncertain, the pore morphology characterization technique using the Euler number and shape factor is applicable to all types of digital cores. In addition, this characterization technique can be extended to other unconventional rocks and even explore its impact on multiphase flow to further enhanced hydrocarbon recovery.

4. CONCLUSIONS

This work analyzed the pore morphology and permeability of heterogeneous sandstone using micro-CT. The Euler number and shape factor were introduced to quantitively characterize the pore topology and shape, respectively. The relationships between the Euler number, shape factor, fractal dimension, and surface area were further analyzed, and the influence of the pore morphology on the permeability was clarified based on the modified KC equation. The following conclusions are drawn.

(1) The Euler number and shape factor are found to be closely related to the pore diameter through pore size distribution analysis. The pore shape in the pore diameter range of 0−50 μm is approximately spherical. The average Euler number is 0.96 with a 0−100 μm pore diameter, and the corresponding pore structure is relatively complete. The pore shape and topology of large diameter pores are complex, and the morphological differences between different pores are significant.

(2) In the connected pore system, the larger the porosity, the more complex the pore shape and topology are, resulting in a larger pore surface area and fractal dimension. The shape factor, surface area, and fractal dimension are positively correlated, and they are negatively correlated with the Euler number.

(3) The modified KC equation can characterize the permeability using the Euler number and shape factor. The permeability has a negative correlation with the shape factor and Euler number under constant porosity. The increase of the Euler number will increase the pore heterogeneity and decrease the permeability. Furthermore, the shape factor has a more obvious impact on permeability and decreases with increasing Euler number.

AUTHOR INFORMATION

Corresponding Author

Jianchao Cai − *State Key Laboratory of Petroleum Resources and Prospecting, China University of Petroleum, Beijing 102249, P. R. China;* orcid.org/0000-0003-2950-888X; Email: caijc@cup.edu.cn

Authors

Xiangjie Qin − *State Key Laboratory of Petroleum Resources and Prospecting, China University of Petroleum, Beijing 102249, P. R. China*

Yuxuan Xia − *Institute of Geophysics and Geomatics, China University of Geosciences, Wuhan 430074, P. R. China*

Jinsui Wu − *Department of Safety Engineering, North China Institute of Science and Technology, Beijing 101601, P. R. China*

Chenhao Sun − *State Key Laboratory of Petroleum Resources and Prospecting, China University of Petroleum, Beijing 102249, P. R. China*

Jianhui Zeng − *State Key Laboratory of Petroleum Resources and Prospecting, China University of Petroleum, Beijing 102249, P. R. China;* orcid.org/0000-0002-2453-4512

Kai Xu − *State Key Laboratory of Petroleum Resources and Prospecting, China University of Petroleum, Beijing 102249, P. R. China*

Complete contact information is available at: https://pubs.acs.org/10.1021/acs.energyfuels.2c01359

Notes

The authors declare no competing financial interest.

ACKNOWLEDGMENTS

This work was supported from the National Natural Science Foundation of China (No. 42172159) and the Fundamental Research Funds for the Central Universities (No. 2462021YXZZ005).

NOMENCLATURE

A	pore surface area, μm^2
A_n	anisotropy
D	fractal dimension
E	3D Euler number
h	fitting parameter
K	permeability, μm^2
K_c	Kozeny−Carman constant
l	fitting parameter
m	fitting parameter
M	specific surface area, $\mu m^2/\mu m^3$
n	fitting parameter
N	number of boxes
p	maximum number of r dimensional closed chains
r	spatial dimension
r_{12}	correlation coefficient between x_1 and x_2
r_{13}	correlation coefficient between x_1 and x_3
r_{23}	correlation coefficient between x_2 and x_3
$r_{12(3)}$	correlation coefficient between x_1 and x_2 after removing the influence of x_3
S	shape factor
V	model volume, μm^3
V_p	pore volume, μm^3
x	spatial target
x_1	variable

https://doi.org/10.1021/acs.energyfuels.2c01359
Energy Fuels 2022, 36, 7519−7530

x_2 variable
x_3 variable
β_0 number of isolated components
β_1 number of channels
β_2 number of closed cavities
ε side length of cube box
λ_{min} minimum eigenvalue
λ_{max} maximum eigenvalue
φ porosity
χ Euler number of spatial target x

REFERENCES

(1) Valvatne, P. H.; Blunt, M. J. Predictive Pore-Scale Modeling of Two-Phase Flow in Mixed Wet Media. *Water Resour. Res.* **2004**, *40*, W07406.

(2) Zhang, Y.; Zeng, L.; Luo, Q.; Zhu, R.; Lyu, W.; Liu, D.; Dai, Q.; Pan, S. Influence of Natural Fractures on Tight Oil Migration and Production: A Case Study of Permian Lucaogou Formation in Jimsar Sag, Junggar Basin, NW China. *J. Earth Sci.* **2021**, *32* (4), 927−945.

(3) Lai, J.; Wang, G.; Wang, Z.; Chen, J.; Pang, X.; Wang, S.; Zhou, Z.; He, Z.; Qin, Z.; Fan, X. A Review on Pore Structure Characterization in Tight Sandstones. *Earth-Sci. Rev.* **2018**, *177*, 436−457.

(4) Cao, Y.; Tang, M.; Zhang, Q.; Tang, J.; Lu, S. Dynamic Capillary Pressure Analysis of Tight Sandstone Based on Digital Rock Model. *Capillarity* **2020**, *3* (2), 28−35.

(5) Meng, T.; Yongbing, X.; Ma, J.; Yue, Y.; Liu, W.; Zhang, J.; Erbing, L. Evolution of Permeability and Microscopic Pore Structure of Sandstone and Its Weakening Mechanism under Coupled Thermo-Hydro-Mechanical Environment Subjected to Real-Time High Temperature. *Eng. Geol.* **2021**, *280*, 105955.

(6) Zhong, X.; Zhu, Y.; Jiao, T.; Qi, Z.; Luo, J.; Xie, Y.; Liu, L. Microscopic Pore Throat Structures and Water Flooding in Heterogeneous Low-Permeability Sandstone Reservoirs: A Case Study of the Jurassic Yan'an Formation in the Huanjiang Area, Ordos Basin, Northern China. *J. Asian Earth Sci.* **2021**, *219*, 104903.

(7) Zhao, J.; Wang, F.; Cai, J. 3D Tight Sandstone Digital Rock Reconstruction with Deep Learning. *J. Pet. Sci. Eng.* **2021**, *207*, 109020.

(8) Chen, L.; He, A.; Zhao, J.; Kang, Q.; Li, Z.; Carmeliet, J.; Shikazono, N.; Tao, W. Pore-Scale Modeling of Complex Transport Phenomena in Porous Media. *Prog. Energy Combust. Sci.* **2022**, *88*, 100968.

(9) Yi, J.; Xing, H.; Wang, J.; Xia, Z.; Jing, Y. Pore-Scale Study of the Effects of Surface Roughness on Relative Permeability of Rock Fractures Using Lattice Boltzmann Method. *Chem. Eng. Sci.* **2019**, *209*, 115178.

(10) Ju, Y.; Gong, W.; Chang, W.; Sun, M. Effects of Pore Characteristics on Water-Oil Two-Phase Displacement in Non-Homogeneous Pore Structures: A Pore-Scale Lattice Boltzmann Model Considering Various Fluid Density Ratios. *Int. J. Eng. Sci.* **2020**, *154*, 103343.

(11) Shan, L.; Bai, X.; Liu, C.; Feng, Y.; Liu, Y.; Qi, Y. Super-Resolution Reconstruction of Digital Rock CT Images Based on Residual Attention Mechanism. *Adv. Geo-Energy Res.* **2022**, *6* (2), 157−168.

(12) Zhao, Y.; Sun, Y.; Yuan, L.; Xu, Q. Impact of Nanopore Structure on Coal Strength: A Study Based on Synchrotron Radiation Nano-CT. *Results Phys.* **2020**, *17*, 103029.

(13) Yang, Y.; Tao, L.; Iglauer, S.; Hejazi, S. H.; Yao, J.; Zhang, W.; Zhang, K. Quantitative Statistical Evaluation of Micro Residual Oil after Polymer Flooding Based on X-Ray Micro Computed-Tomography Scanning. *Energy Fuels* **2020**, *34* (9), 10762−10772.

(14) Chen, J.; Cheng, W.; Wang, G.; Li, H. Effect of Dominated Coal Pores and Fractures on Water Migration after Low-Pressure Water Injection Based on CT Images. *Fuel* **2022**, *307*, 121795.

(15) Munawar, M. J.; Lin, C.; Cnudde, V.; Bultreys, T.; Dong, C.; Zhang, X.; De Boever, W.; Zahid, M. A.; Wu, Y. Petrographic Characterization to Build an Accurate Rock Model Using Micro-CT: Case Study on Low-Permeable to Tight Turbidite Sandstone from Eocene Shahejie Formation. *Micron* **2018**, *109*, 22−33.

(16) Su, Y.; Zha, M.; Jiang, L.; Ding, X.; Qu, J.; Jin, J.; Iglauer, S. Pore Structure and Fluid Distribution of Tight Sandstone by the Combined Use of SEM, MICP and X-Ray Micro-CT. *J. Pet. Sci. Eng.* **2022**, *208*, 109241.

(17) Garum, M.; Glover, P. W. J.; Lorinczi, P.; Drummond-Brydson, R.; Hassanpour, A. Micro- and Nano-Scale Pore Structure in Gas Shale Using Xμ-CT and FIB-SEM Techniques. *Energy Fuels* **2020**, *34* (10), 12340−12353.

(18) Chandra, D.; Vishal, V. A Critical Review on Pore to Continuum Scale Imaging Techniques for Enhanced Shale Gas Recovery. *Earth-Sci.Rev.* **2021**, *217*, 103638.

(19) Yao, Y.; Liu, D.; Xie, S. Quantitative Characterization of Methane Adsorption on Coal Using a Low-Field NMR Relaxation Method. *Int. J. Coal Geol.* **2014**, *131*, 32−40.

(20) Zhu, D. Y.; Deng, Z. H.; Chen, S. W. A Review of Nuclear Magnetic Resonance (NMR) Technology Applied in the Characterization of Polymer Gels for Petroleum Reservoir Conformance Control. *Pet. Sci.* **2021**, *18* (6), 1760−1775.

(21) Houben, M. E.; Desbois, G.; Urai, J. L. A Comparative Study of Representative 2D Microstructures in Shaly and Sandy Facies of Opalinus Clay (Mont Terri, Switzerland) Inferred Form BIB-SEM and MIP Methods. *Mar. Pet. Geol.* **2014**, *49*, 143−161.

(22) Wang, D.; Zhang, P.; Wei, J.; Yu, C. The Seepage Properties and Permeability Enhancement Mechanism in Coal under Temperature Shocks during Unloading Confining Pressures. *J. Nat. Gas Sci. Eng.* **2020**, *77*, 103242.

(23) Zha, W.; Li, X.; Xing, Y.; He, L.; Li, D. Reconstruction of Shale Image Based on Wasserstein Generative Adversarial Networks with Gradient Penalty. *Adv. Geo-Energy Res.* **2020**, *4* (1), 107−114.

(24) Wang, Z.; Li, H.; Lan, X.; Wang, K.; Yang, Y.; Lisitsa, V. Formation Damage Mechanism of a Sandstone Reservoir Based on Micro-Computed Tomography. *Adv. Geo-Energy Res.* **2021**, *5* (1), 25−38.

(25) Busse, J.; de Dreuzy, J. R.; Galindo Torres, S.; Bringemeier, D.; Scheuermann, A. Image Processing Based Characterisation of Coal Cleat Networks. *Int. J. Coal Geol.* **2017**, *169*, 1−21.

(26) Wang, X.; Pan, J.; Wang, K.; Ge, T.; Wei, J.; Wu, W. Characterizing the Shape, Size, and Distribution Heterogeneity of Pore-Fractures in High Rank Coal Based on X-Ray CT Image Analysis and Mercury Intrusion Porosimetry. *Fuel* **2020**, *282*, 118754.

(27) Schmitt Rahner, M.; Halisch, M.; Peres Fernandes, C.; Weller, A.; Sampaio Santiago dos Santos, V. Fractal Dimensions of Pore Spaces in Unconventional Reservoir Rocks Using X-Ray Nano- and Micro-Computed Tomography. *J. Nat. Gas Sci. Eng.* **2018**, *55*, 298−311.

(28) Armstrong, R. T.; McClure, J. E.; Berrill, M. A.; Rücker, M.; Schlüter, S.; Berg, S. Beyond Darcy's Law: The Role of Phase Topology and Ganglion Dynamics for Two-Fluid Flow. *Phys. Rev. E* **2016**, *94*, 043113.

(29) Li, J.; Jiang, H.; Wang, C.; Zhao, Y.; Gao, Y.; Pei, Y.; Wang, C.; Dong, H. Pore-Scale Investigation of Microscopic Remaining Oil Variation Characteristics in Water-Wet Sandstone Using CT Scanning. *J. Nat. Gas Sci. Eng.* **2017**, *48*, 36−45.

(30) Guo, C.; Wang, X.; Wang, H.; He, S.; Liu, H.; Zhu, P. Effect of Pore Structure on Displacement Efficiency and Oil-Cluster Morphology by Using Micro Computed Tomography (MCT) Technique. *Fuel* **2018**, *230*, 430−439.

(31) Yang, Y.; Yang, H.; Tao, L.; Yao, J.; Wang, W.; Zhang, K.; Luquot, L. Microscopic Determination of Remaining Oil Distribution in Sandstones with Different Permeability Scales Using Computed Tomography Scanning. *J. Energy Resour. Technol.* **2019**, *141* (9), 092903.

(32) Davudov, D.; Moghanloo, R. G.; Zhang, Y. Interplay between Pore Connectivity and Permeability in Shale Sample. *Int. J. Coal Geol.* **2020**, *220*, 103427.

(33) Guo, C.; Cui, Y. Pore Structure Characteristics of Debris Flow Source Material in the Wenchuan Earthquake Area. *Eng. Geol.* **2020**, *267*, 105499.

https://doi.org/10.1021/acs.energyfuels.2c01359
Energy Fuels 2022, 36, 7519−7530

(34) Mostaghimi, P.; Blunt, M. J.; Bijeljic, B. Computations of Absolute Permeability on Micro-CT Images. *Math. Geosci.* **2013**, *45* (1), 103−125.
(35) Alhammadi, A. M.; Gao, Y.; Akai, T.; Blunt, M. J.; Bijeljic, B. Pore-Scale X-Ray Imaging with Measurement of Relative Permeability, Capillary Pressure and Oil Recovery in a Mixed-Wet Micro-Porous Carbonate Reservoir Rock. *Fuel* **2020**, *268*, 117018.
(36) Wang, G.; Shen, J.; Liu, S.; Jiang, C.; Qin, X. Three-Dimensional Modeling and Analysis of Macro-Pore Structure of Coal Using Combined X-Ray CT Imaging and Fractal Theory. *Int. J. Rock Mech. Min. Sci.* **2019**, *123*, 104082.
(37) Yang, Y.; Wang, K.; Zhang, L.; Sun, H.; Zhang, K.; Ma, J. Pore-Scale Simulation of Shale Oil Flow Based on Pore Network Model. *Fuel* **2019**, *251*, 683−692.
(38) Ebrahimi Khabbazi, A.; Ellis, J. S.; Bazylak, A. Developing a New Form of the Kozeny−Carman Parameter for Structured Porous Media through Lattice-Boltzmann Modeling. *Comput. Fluids* **2013**, *75*, 35−41.
(39) Guo, Z.; Fang, Q.; Nong, M.; Ren, X. A Novel Kozeny-Carman-Based Permeability Model for Hydrate-Bearing Sediments. *Energy* **2021**, *234*, 121203.
(40) Liu, L.; Sun, Q.; Wu, N.; Liu, C.; Ning, F.; Cai, J. Fractal Analyses of the Shape Factor in Kozeny-Carman Equation for Hydraulic Permeability in Hydrate-Bearing Sediments. *Fractals* **2021**, *29* (7), 2150217.
(41) Safari, M.; Gholami, R.; Jami, M.; Ananthan, M. A.; Rahimi, A.; Khur, W. S. Developing a Porosity-Permeability Relationship for Ellipsoidal Grains: A Correction Shape Factor for Kozeny-Carman's Equation. *J. Pet. Sci. Eng.* **2021**, *205*, 108896.
(42) Shah, A.; Bangash, J. I.; Khan, A. W.; Ahmed, I.; Khan, A.; Khan, A.; Khan, A. Comparative Analysis of Median Filter and Its Variants for Removal of Impulse Noise from Gray Scale Images. *J. King Saud Univ. - Comput. Inf. Sci.* **2022**, *34* (3), 505−519.
(43) Guerroudji, M. A.; Ameur, Z. A New Approach for the Detection of Mammary Calcifications by Using the White Top-Hat Transform and Thresholding of Otsu. *Optik (Stuttg).* **2016**, *127* (3), 1251−1259.
(44) Zakirov, T.; Galeev, A. Absolute Permeability Calculations in Micro-Computed Tomography Models of Sandstones by Navier-Stokes and Lattice Boltzmann Equations. *Int. J. Heat Mass Transfer* **2019**, *129*, 415−426.
(45) Hu, C.; Liu, X.; Jia, Y.; Duan, Z. Permeability Anisotropy of Methane Hydrate-Bearing Sands: Insights from CT Scanning and Pore Network Modelling. *Comput. Geotech.* **2020**, *123*, 103568.
(46) Lv, J.; Cheng, Z.; Xue, K.; Liu, Y.; Mu, H. Pore-Scale Morphology and Wettability Characteristics of Xenon Hydrate in Sand Matrix - Laboratory Visualization with Micro-CT. *Mar. Pet. Geol.* **2020**, *120*, 104525.
(47) Diaz-De-Leon, S. J. L.; Sossa-Azuela, J. H. On the Computation of the Euler Number of a Binary Object. *Pattern Recognit.* **1996**, *29* (3), 471−476.
(48) Ziou, D.; Allili, M. Generating Cubical Complexes from Image Data and Computation of the Euler Number. *Pattern Recognit.* **2002**, *35* (12), 2833−2839.
(49) Zhou, Y.; Wu, S.; Li, Z.; Zhu, R.; Xie, S.; Zhai, X.; Lei, L. Investigation of Microscopic Pore Structure and Permeability Prediction in Sand-Conglomerate Reservoirs. *J. Earth Sci.* **2021**, *32* (4), 818−827.
(50) Cui, G.; Wei, J.; Feng, X.-T.; Liu, J.; Elsworth, D.; Chen, T.; Xiong, W. Preliminary Study on the Feasibility of Co-Exploitation of Coal and Uranium. *Int. J. Rock Mech. Min. Sci.* **2019**, *123*, 104098.
(51) Tian, Z.; Wei, W.; Zhou, S.; Wood, D. A.; Cai, J. Experimental and Fractal Characterization of the Microstructure of Shales from Sichuan Basin, China. *Energy Fuels* **2021**, *35* (5), 3899−3914.
(52) Kozeny, J. Uber Kapillare Leitung Des Wasser Im Boden. *Sitzungsber Akad. Wiss., Wien* **1927**, *136* (2a), 271−306.
(53) Carman, P. C. Fluid Flow through Granular Beds. *Chem. Eng. Res. Des.* **1997**, *75*, S32−S48.
(54) Cai, J.; Luo, L.; Ye, R.; Zeng, X.; Hu, X. Recent Advances on Fractal Modeling of Permeability for Fibrous Porous Media. *Fractals* **2015**, *23* (1), 1540006.
(55) Saxena, N.; Hows, A.; Hofmann, R.; Alpak, F. O.; Dietderich, J.; Appel, M.; Freeman, J.; De Jong, H. Rock Properties from Micro-CT Images: Digital Rock Transforms for Resolution, Pore Volume, and Field of View. *Adv. Water Resour.* **2019**, *134*, 103419.

https://doi.org/10.1021/acs.energyfuels.2c01359
Energy Fuels 2022, 36, 7519−7530